AGU PUBLICATIONS

JGR

Journal of Geophysical Research: Solid Earth

RESEARCH ARTICLE

10.1002/2016JB012863

Key Points:

- Al substitution greatly affected the magnetic properties of Al-magnetite
- Surficial micropores of Al-magnetite samples could serve as a practical fingerprint of high-temperature mineralogical alteration processes
- The correlation between T_c and B_c can be used to discriminate titanomagnetite from Al-magnetite

Supporting Information:

- Supporting Information S1

Correspondence to:
Q. Liu,
liux0272@yahoo.com

Citation:
Jiang, Z., Q. Liu, X. Zhao, A. P. Roberts, D. Heslop, V. Barrón, and J. Torrent (2016), Magnetism of Al-substituted magnetite reduced from Al-hematite, *J. Geophys. Res. Solid Earth*, *121*, doi:10.1002/2016JB012863.

Received 27 JAN 2016
Accepted 4 JUN 2016
Accepted article online 7 JUN 2016

Magnetism of Al-substituted magnetite reduced from Al-hematite

Zhaoxia Jiang[1,2,3], Qingsong Liu[1,2], Xiang Zhao[3], Andrew P. Roberts[3], David Heslop[3], Vidal Barrón[4], and José Torrent[4]

[1]State Key Laboratory of Lithospheric Evolution, Institute of Geology and Geophysics, Chinese Academy of Sciences, Beijing, China, [2]Laboratory for Marine Geology, Qingdao National Oceanography Laboratory for Marine Science and Technology, Qingdao, China, [3]Research School of Earth Sciences, Australian National University, Canberra, ACT, Australia, [4]Departamento de Agronomía, Universidad de Córdoba, Córdoba, Spain

Abstract Aluminum-substituted magnetite (Al-magnetite) reduced from Al-substituted hematite or goethite (Al-hematite or Al-goethite) is an environmentally important constituent of magnetically enhanced soils. In order to characterize the magnetic properties of Al-magnetite, two series of Al-magnetite samples were synthesized through reduction of Al-hematite by a mixed gas (80% CO_2 and 20% CO) at 395°C for 72 h in a quartz tube furnace. Al-magnetite samples inherited the morphology of their parent Al-hematite samples, but only those transformed from Al-hematite synthesized at low temperature possessed surficial micropores, which originated from the release of structural water during heating. Surface micropores could thus serve as a practical fingerprint of fire or other high-temperature mineralogical alteration processes in natural environments, e.g., shear friction in seismic zones. In addition, Al substitution greatly affects the magnetic properties of Al-magnetite. For example, coercivity (B_c) increases with increasing Al content and then decreases slightly, while the saturation magnetization (M_s), Curie temperature (T_c), and Verwey transition temperature (T_v) all decrease with increasing Al content due to crystal defect formation and dilution of magnetic ions caused by Al incorporation. Moreover, different trends in the correlation between T_c and B_c can be used to discriminate titanomagnetite from Al-magnetite, which is likely to be important in environmental and paleomagnetic studies, particularly in soil.

1. Introduction

Magnetite has a strong magnetic moment and is one of the most commonly detected magnetic minerals in modern soils [e.g., *Dearing et al.*, 1997; *Geiss and Zanner*, 2006; *Geiss et al.*, 2008] and in lacustrine [e.g., *Snowball*, 1994; *Gibbs-Eggar et al.*, 1999; *Ortega et al.*, 2006] and marine sediments [e.g., *Bailey et al.*, 2011; *Oliva-Urcia et al.*, 2011; *Roberts et al.*, 2012, 2013]. Detrital magnetite from atmospheric dust, rivers, and local parent materials [e.g., *Duce et al.*, 1980; *Glasby*, 1991; *Prospero et al.*, 2002], and authigenic magnetite [e.g., *Oldfield*, 1992, 2007] are two principal sources of magnetite in soils and sediments. Authigenic magnetite can form either from biogenic processes by bacteria in the water column or in sediments [*Blakemore et al.*, 1985; *Lovley et al.*, 1987; *Snowball*, 1994; *Guyodo et al.*, 2006] or from abiotic chemical processes without the participation of organisms [*Mullins*, 1977; *Taylor*, 1987; *Schwertmann*, 1988; *Maher and Taylor*, 1989; *Zhou et al.*, 1990; *Dearing et al.*, 1997]. The primary reactions through which magnetite are introduced into the pedogenic cycle involve hydrolytic and iron transformation of lithogenic Fe(II)-containing primary minerals (mainly Fe(II) silicates) ($Fe_2SiO_4 + O_2 + H_2O \rightarrow Fe_5HO_8$ (ferrihydrite) $+ Fe^{2+} + H_2O \rightarrow Fe_3O_4 + H^+$) [*Taylor*, 1987; *Schwertmann*, 1988] or by weathering of iron silicate or carbonate [*Mullins*, 1977; *Evans and Heller*, 2003].

Previous studies have shown that reduction of hematite and goethite is also an important process that gives rise to magnetite formation in surface soils or sediments [*Tite and Mullins*, 1971; *Kletetschka and Banerjee*, 1995; *Gedye et al.*, 2000; *Bloemendal and Liu*, 2005; *Geiss et al.*, 2008; *Nie et al.*, 2010]. For example, a fire can heat the topmost centimeters of soil to 800°C and cause a reducing soil-pore atmosphere, e.g., CO and CO_2 [*Tunstall et al.*, 1976; *Haliuc et al.*, 2016], which results in transformation of hematite and/or goethite to magnetite [*Swann and Tighe*, 1977; *Zhang et al.*, 2012; *Jiang et al.*, 2015]. In addition, underground burning can reach much higher temperatures, e.g., underground peat and coal fires, so that metallic Fe can be formed [*de Boer et al.*, 2001]. Organic carbon and some clay minerals are effective reducing agents in soils [*Hanesch et al.*, 2006; *Zhang et al.*, 2012; *Jiang et al.*, 2015]. *Hanesch et al.* [2006] showed that weakly magnetic minerals (hematite, goethite, and ferrihydrite) or paramagnetic minerals (e.g., siderite) in soils and sediments can transform into magnetite or maghemite in the presence of organic carbon during heating. Clay minerals can have a similar effect where the reducing ability of chlorite and illite are stronger than that of kaolinite and smectite [*Zhang et al*., 2012; *Jiang et al*., 2015]. Moreover, neoformed magnetite has also been detected in fault gouge [*Hirono et al*., 2006; *Han et al*., 2007; *Tanikawa et al*., 2007; *Mishima et al*., 2009; *Yang et al*., 2012], where frictional heating is generated by shear friction at high slip rates during large earthquakes [*Scholz*, 2002]. Rapidly elevated temperatures (up to 1000°C) within the fault slip zone induce thermochemical reactions, such as decomposition of hematite and clay minerals [*Enomoto and Zheng*, 1998; *Ferré et al*., 2005; *Fukuchi et al*., 2005; *Tanikawa et al*., 2007, 2008], where the temperature depends on the distance to the slip surface [*Yang et al*., 2016]. Therefore, systematic investigation of magnetite that was produced at low temperatures in natural environments should assist in understanding environmental magnetic signals in tropical soils and sediments.

Due to the prevalence of Al substitution in natural hematite and goethite [*Schwertmann et al*., 1977; *Cornell and Schwertmann*, 2003], magnetite produced by reduction of these phases may also be Al substituted. Lithogenic magnetite is usually low in, or free from, Al [*Allan et al*., 1989], but clay-sized magnetite in soils may be Al substituted (i.e., 0.05–0.16 mol%), which may indicate that it precipitated through hydrolytic transformation of lithogenic Fe(II)-containing primary minerals (mainly Fe(II) silicates) in an Al-containing soil solution [*Schwertmann*, 1988; *Schwertmann and Murad*, 1990; *Da Costa et al*., 1999]. Mixtures of Al-magnetite and partially oxidized Al-magnetite have been detected in a soil developed from basalt [*Goulart et al*., 1998]. Previous studies have investigated the influence of cation substitution (e.g., Ti, Zn, and Co) on the magnetic properties of magnetite [*Brabers et al*., 1998; *Yu et al*., 2013; *Zélis et al*., 2013; *Saha et al*., 2014]. In particular, Ti-substituted magnetite (titanomagnetite) has received much attention because it is prevalent in basalts and is a widespread carrier of paleomagnetic signals [*Akimoto et al*., 1957; *Nagata*, 1962; *O'Reilly and Banerjee*, 1966; *Readman and O'Reilly*, 1971; *Bleil and Petersen*, 1983; *Zhou et al*., 1997; *Carter-Stiglitz et al*., 2006; *Pan et al*., 2006]. However, fewer investigations have been made of Al-magnetite and are restricted to studies of magnetostriction [*Brabers and Hendrinks*, 1982] and the Verwey transition [*Brabers et al*., 1998]. For example, the Verwey temperature shifts as a function of Al concentration in magnetite [*Brabers et al*., 1998].

In this study, we reduced Al-hematite samples with varying Al content to form Al-magnetite by heating to 395°C [*Özdemir and Dunlop*, 2010]. The mineralogical and magnetic properties of the resulting Al-magnetites were investigated systematically, and the implications of Al-magnetite formation for paleomagnetic and environmental magnetic studies are discussed.

2. Samples and Experiments

Al-magnetite samples were produced by reduction of two series of Al-hematite samples. The first Al-hematite sample series (HFh0, HFh2, HFh4, HFh8, and HFh16) was produced by transformation from ferrihydrite at ~95°C in solution [*Jiang et al*., 2012], and the other parent sample series (Hm0, Hm4, Hm6, Hm8, Hm10, Hm14, Hm16, and Hm20) was transformed from goethite at 600°C [*Jiang et al*., 2014]. Al-hematite powders were put into ceramic boxes and fixed in the middle zone of a quartz tube furnace. The tube was flushed with purified N_2 gas for an hour to remove oxygen before heating. The samples were then reduced in a mixed gas of 80% CO_2 and 20% CO at 395°C for 72 h (supporting information Figure S1) [*Özdemir and Dunlop*, 2010]. Finally, two Al-magnetite sample series (Series I-0, I-2, I-4, I-8, and I-16 and Series II-0, II-4, II-8, II-10, II-14, II-16, and II-20) were produced. Detailed sample information is summarized in Table 1.

The purity of our samples was determined by powder X-ray diffraction (XRD) patterns, which were measured using a D/MAX-2400 XRD instrument with monochromatized Cu*Kα* radiation operating at 40 kV and 40 mA. Diffraction patterns were measured through the 20–70° 2θ range at a scan speed of 0.0167° 2θ/s with a 0.1 mm divergence slit size. The lattice parameter of samples was determined with the JADE 6.5 software. Transmission electron microscope (TEM) images were obtained with a JEM-2010 microscope operating at 100 kV to investigate particle morphology and grain size variation with Al content.

Magnetic hysteresis loops of samples packed into gelcaps were measured over a field range of ± 1 T using a vibrating sample magnetometer (MicroMag™ VSM 3900). The saturation magnetization (M_s), saturation

Table 1. Summary Information for the Two Series of Al-Magnetite Samples[a]

Sample	Al Content	Precursor	a (Å)	Error	Particle Size (nm)	Error	B_c (mT)	B_{cr} (mT)	M_r (Am^2/kg)	M_s (Am^2/kg)	B_{cr}/B_c	M_r/M_s	T_c (°C)	T_v (K)
I-0	0	HFh0	8.38	0.001	200	31	20.5	35.9	23.3	86.6	1.75	0.27	580.0	120.0
I-2	2.03	HFh2	8.39	0.002	291	53	34.5	56.3	25.0	72.1	1.63	0.35	562.0	
I-4	3.88	HFh4	8.36	0.001	246	42	27.4	40.8	29.8	77.8	1.49	0.38	543.0	116.0
I-8	6.81	HFh8	8.37	0.001	354	53	27.4	39.3	22.3	57.5	1.43	0.39	548.0	96.0
I-16	12.94	HFh16	8.36	0.001	338	71	18.6	20.7	4.8	19.6	1.11	0.24	541.0	
II-0	0	Hm0	8.40	2E–04	223	58	15.6	27.9	19.5	90.0	1.79	0.20	576.8	120.0
II-4	4.20	Hm4	8.36	9E–04	139	29	22.5	39.5	21.3	79.3	1.76	0.27		116.0
II-8	8.40	Hm8	8.36	0.001	115	35	23.5	38.5	22.1	68.8	1.64	0.32	534.0	
II-10	9.10	Hm10	8.35	0.001	85	20	21.2	33.6	24.1	73.6	1.58	0.33		111.0
II-14	12.40	Hm14			65	13	23.2	35.2	19.2	53.3	1.52	0.36		106.0
II-16	14.20	Hm16	8.34	0.001	57	15	22.1	33.8	17.7	48.2	1.53	0.37	537.4	111.0
II-20	16.90	Hm20	8.34	0.001			22.5	34.6	21.3	57.2	1.54	0.37	524.0	

[a]Series I samples (I-0, I-2, I-4, I-8, I-16) were transformed from hematite samples HFh* series, which have been investigated by *Jiang et al.* [2012], and series II samples (II-0, II-4, … , II-20) were transformed from hematite samples Hm* series from *Jiang et al.* [2014]. The unit cell parameter a was calculated based on XRD data. Particle size was measured based on TEM results. Hysteresis parameters (B_c, B_{cr}, M_r, M_s) were acquired from hysteresis loops and back-field demagnetization curves. Curie temperature (T_c) was calculated using the inverse susceptibility method ($1/\chi$) from χ-T curves, and Verwey transition temperature (T_v) was calculated from low-temperature remanence curves.

remanence (M_r), and coercivity (B_c) were determined after paramagnetic slope correction. Stepwise isothermal remanent magnetization (IRM) acquisition and back-field demagnetization curves were also measured up to a maximum field of 1 T to estimate the coercivity of remanence (B_{cr}). These hysteresis parameters are summarized in Table 1. First derivatives of IRM acquisition curves were fitted with coercivity components following *Kruiver et al.* [2001] and *Heslop et al.* [2002]. First-order reversal curve (FORC) measurements were made to investigate the magnetic domain state and extent of magnetostatic interactions in the studied samples using the irregular grid measurement protocol of *Zhao et al.* [2015].

Temperature-dependent magnetic susceptibility (χ-T) curves ranging from room temperature to 700°C were measured using a Kappabridge MFK1-FA system (frequency of 967 Hz, sensitivity of 1×10^{-8} SI, AGICO Ltd., Brno, Czech Republic) in an argon atmosphere. Minor susceptibility contributions from the sample holder and thermocouple were subtracted before estimation of T_c, which was calculated using the inverse susceptibility method ($1/\chi$) [*Petrovský and Kapička*, 2006]. Zero-field cooling (ZFC) curves and room temperature saturation isothermal remanent magnetization (RTSIRM) curves were measured using a Quantum Design Magnetic Properties Measurement System (MPMS XP-5, sensitivity 5.0×10^{-10} Am^2). Samples were first cooled from room temperature to 20 K in zero field and were then exposed to a field of 2.5 T (this saturation IRM is denoted as $SIRM_{20\,K}$). After the magnetic field was switched off, $SIRM_{20\,K}$ was measured from 20 to 300 K at 5 K intervals. In addition, $SIRM_{300\,K}$ was imparted in a 2.5 T field at 300 K. After the magnetic field was switched off, $SIRM_{300\,K}$ was cycled from 300 K to 20 K and then back to 300 K.

3. Results

3.1. Structure and Morphological Properties of Al-Magnetite

TEM images (Figure 1) indicate that the studied Al-magnetites have inherited the morphology of their precursor Al-hematite samples. The morphologies of the Series I samples are similar to those of the precursor Al-hematites, which are platy and have a long-axis length that increases with increasing Al content [*Jiang et al.*, 2012]. Micropores on the surfaces of the Series I Al-magnetite samples are attributed to the release of water from the structure of the original hematite samples. Series II samples are granular and elongated but smaller than those of Series I. No micropores are detected in the surfaces of the Series II samples. Most particles are agglomerated together in the TEM images.

XRD results (Figures 2a and 2b) indicate that the samples from both series consist of magnetite. The characteristic reflections shift slightly to higher 2θ values as Al substitution increases. The lattice parameter, a, and particle size were calculated for all samples based on XRD and TEM results. The lattice parameter for both series decreases with increasing Al substitution because Al^{3+} is a smaller ion than Fe^{3+}. Simultaneously, particle size also varies with Al content, albeit with differing trends in the two series. For Series I, the long-axis length

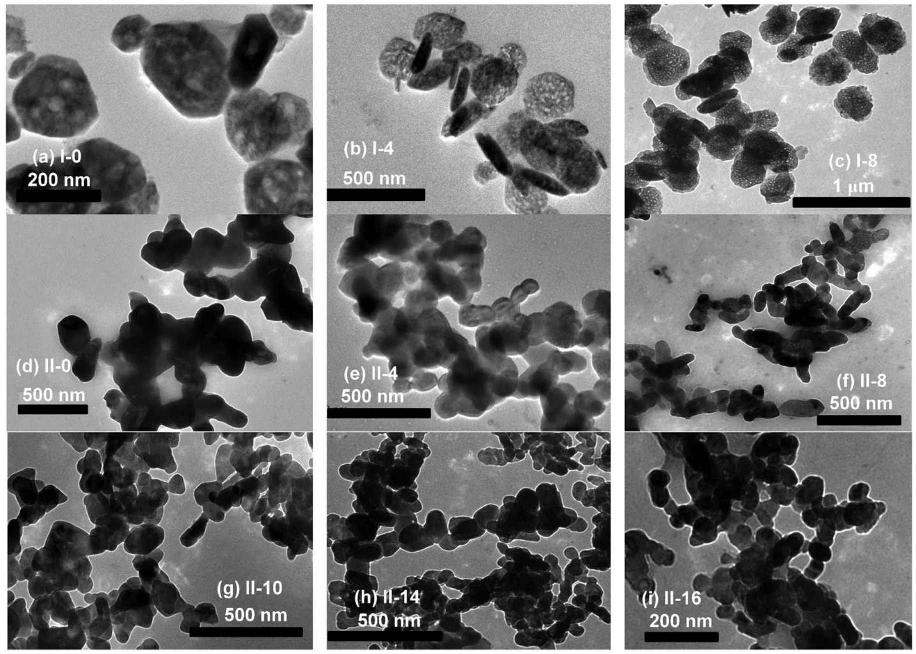

Figure 1. TEM images for representative samples from the two Al-magnetite sample series (I and II), where the number after the series number is the Al content in mol%.

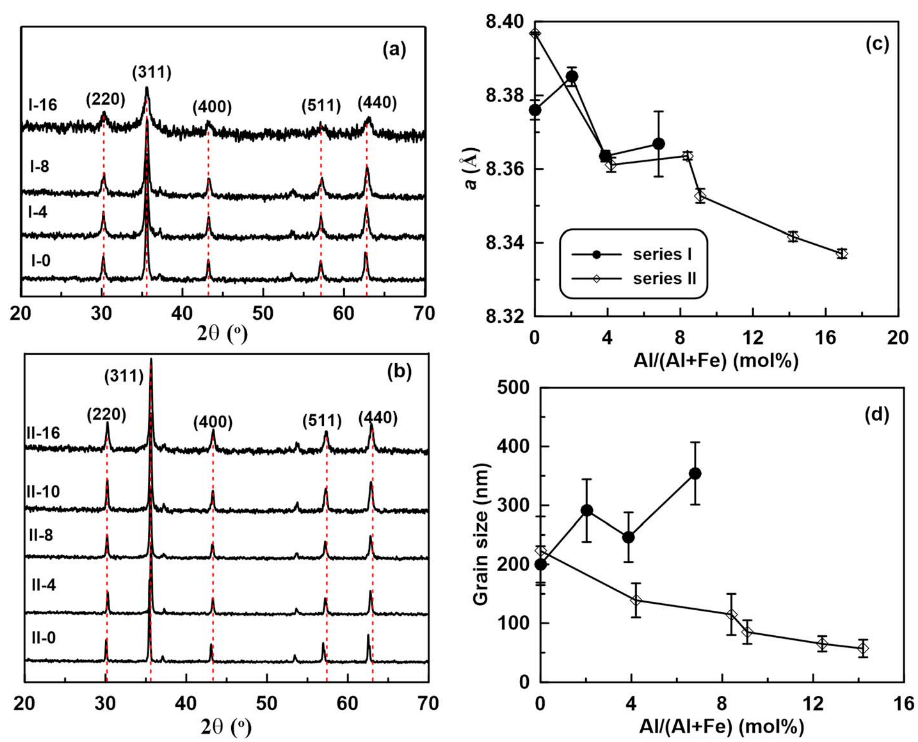

Figure 2. (a, b) XRD data for the two sample series where the red dashed lines represent characteristic reflections for magnetite. (c) Lattice parameter *a*, calculated from XRD data plotted versus Al content and (d) grain size measured on TEM micrographs versus Al content, where solid circles and open diamonds represent data for Series I and II samples, respectively.

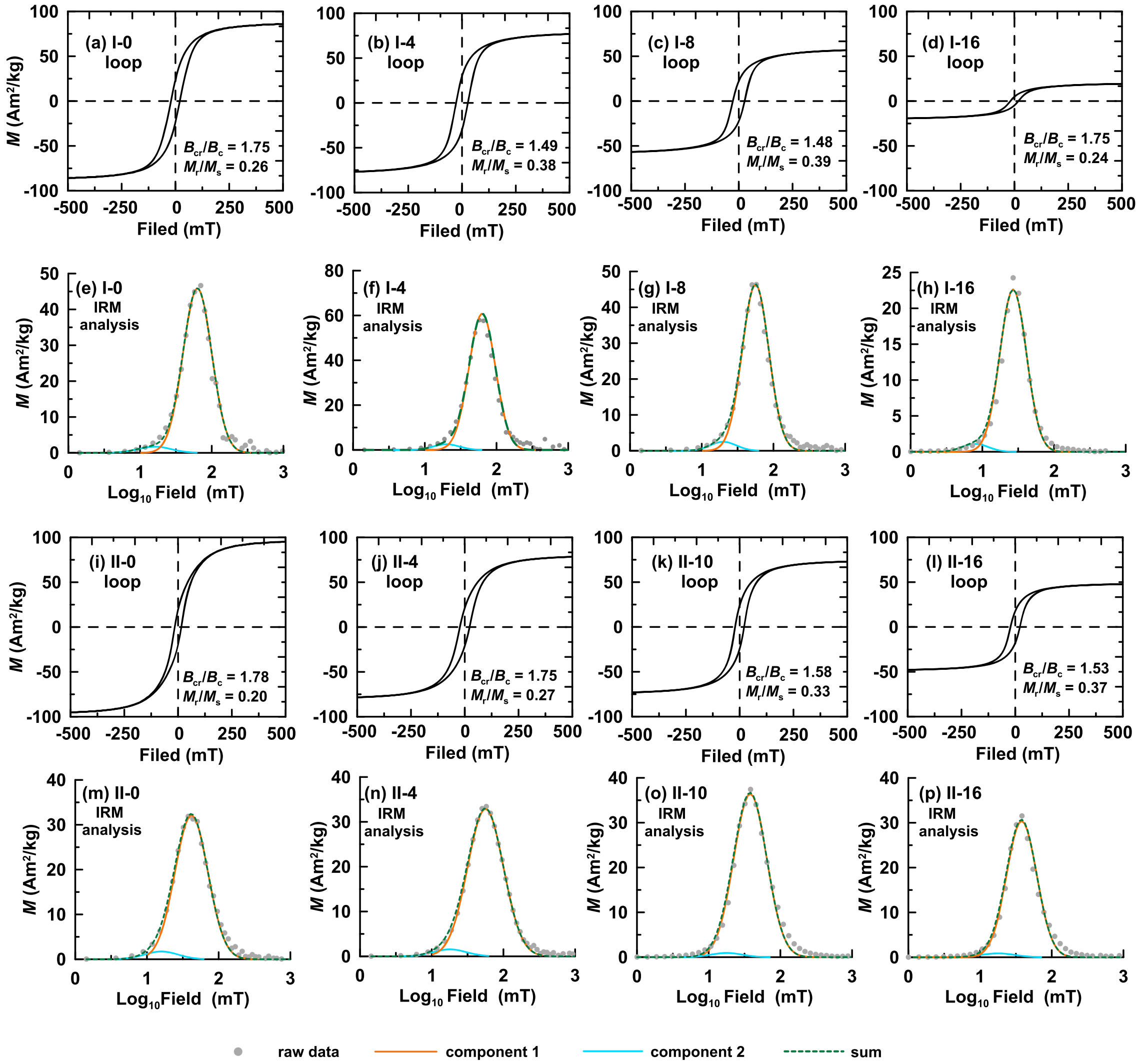

Figure 3. Magnetic results for the two Al-magnetite sample series. (a–d, i–l) Hysteresis loops after paramagnetic slope correction; and (e–h, m–p) coercivity component analysis from IRM acquisition curves, where open circles and green dashed lines represent raw data and the fitted sum of the IRM components, respectively; the orange and blue lines represent the identified components 1 and 2, respectively.

Table 2. IRM Component Analysis of the Al-Magnetite Samples[a]

	Component 1			Component 2		
Sample Name	$B1_{1/2}$ (mT)	DP	IRM Contribution (%)	$B2_{1/2}$ (mT)	DP	IRM Contribution (%)
I-0	63.1	0.20	95.8	15.8	0.23	4.2
I-2	89.1	0.19	94.4	22.4	0.20	5.6
I-4	63.1	0.19	96.1	20.0	0.18	3.9
I-8	56.2	0.19	95.0	20.0	0.18	5.0
I-16	26.9	0.19	95.5	7.9	0.18	4.5
II-0	41.7	0.23	94.9	15.8	0.23	5.1
II-4	56.2	0.25	95.8	17.8	0.23	4.2
II-8	41.7	0.23	98.0	10	0.21	2.0
II-10	38.7	0.23	98.0	17.8	0.21	2.0
II-14	38.0	0.22	99.0	10	0.21	1.0
II-16	38.0	0.21	97.0	17.8	0.23	3.0

[a] $B1_{1/2}$ and $B2_{1/2}$ are the $B_{1/2}$ (mT) values (median field at which half of the SIRM is reached) of coercivity components 1 and 2, respectively. DP is the dispersion parameter for each IRM component. The IRM contribution (%) is the contribution of each IRM component to the total IRM.

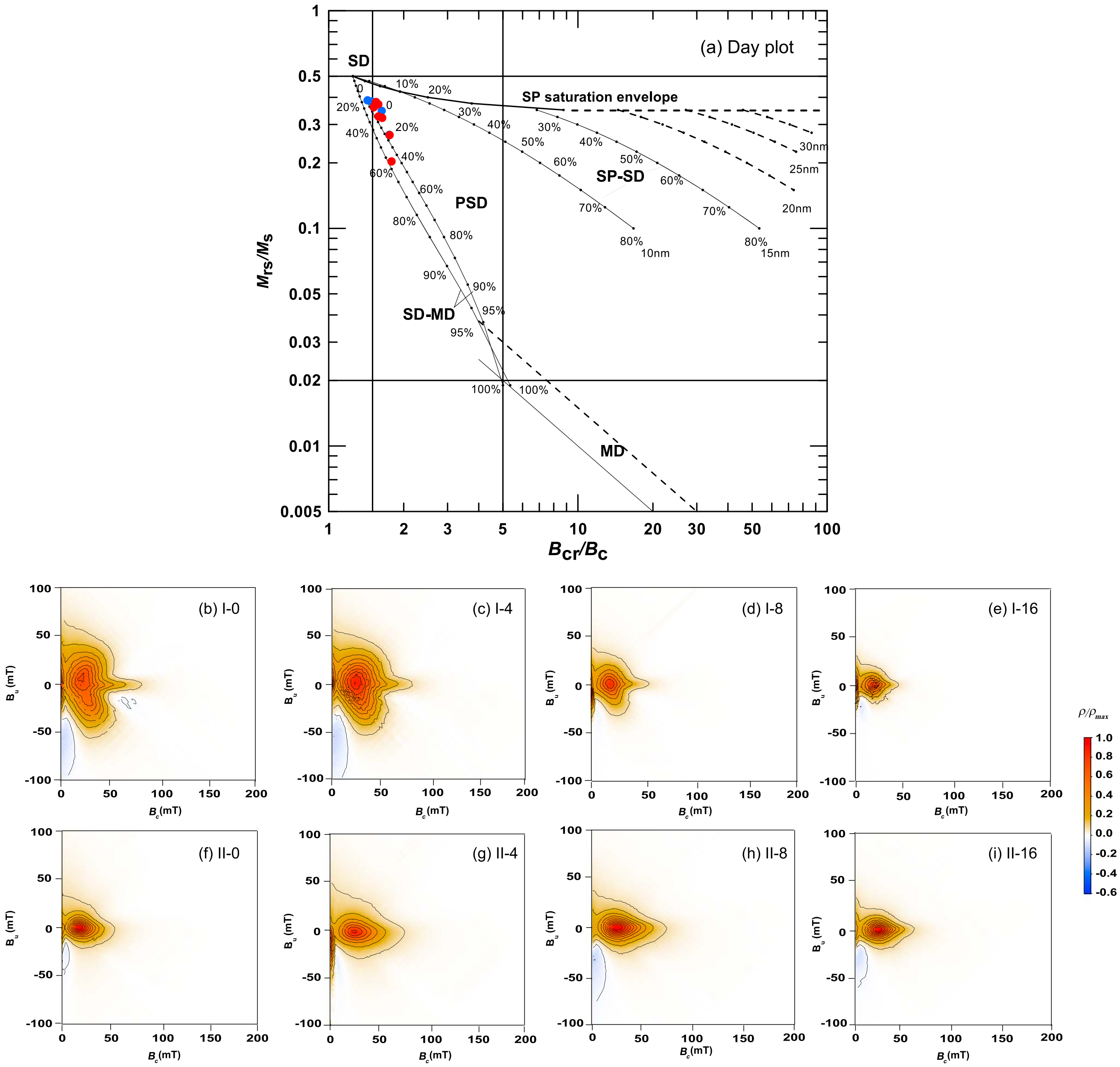

Figure 4. Hysteresis ratios plotted on (a) a Day plot [*Day et al*., 1977; *Dunlop*, 2002], where the blue and red solid circles are data for the series I and II samples, respectively, and the lines represent the boundaries between regions for different domain states and mixing lines (with percentages of the SD end member) for SD + SP and SD + MD mixtures; and (b–i) FORC diagrams for selected samples.

increases with Al content, while that of Series II decreases with Al content. These two trends are consistent with those of the respective precursor Al-hematite samples. *Jiang et al*. [2012] demonstrated that, for hematite, Al substitution can inhibit growth along the crystallographic *z* axis but accelerates growth along the (001) plane. Therefore, as Al content increases, the Series I Al-magnetite particles become thinner and larger. However, for Series II, no anisotropic growth was detected for the precursor hematite samples, and the particle size of the reduced products decreases systematically with increasing Al content.

3.2. Magnetic Properties of Al-Magnetite

Hysteresis results for representative Al-magnetite samples are shown in Figure 3. All samples are saturated below 500 mT and have magnetic properties that are indicative of stable-single-domain-like or slightly finer particles (Figures 3a–3d, 3i–3l). As Al content increases, hysteresis loops become wider, and then narrower, as B_c increases and then decreases. Simultaneously, both M_r and M_s decrease with increasing Al content.

IRM component analyses of representative samples are shown in Figures 3e–3h and 3m–3p and Table 2. Three parameters are used to represent each coercivity component, namely, $B_{1/2}$ (the field at which the component acquires half of its SIRM), DP (the dispersion parameter, which represents the spread of the coercivity distribution), and IRM% (the contribution of the component to the total IRM) [*Kruiver et al*., 2001; *Heslop et al*., 2002]. The DP of a component is controlled by the coercivity distribution, which in turn is related to the grain size distribution. The smaller the DP, the narrower the grain size distribution [*Egli*, 2004]. IRM acquisition curves for representative samples can be fitted with two components, a predominant component with coercivity range from 40 to 60 mT (component 1) and a small component with coercivity around 10–20 mT (component 2). Component 2 contributes less than 5% of the IRM and may represent a thermally activated part of component 1, which causes negatively skewed distributions [*Heslop et al*., 2004]. The DP of component 1 ranges from 0.19 to 0.22, while that of component 2 ranges from 0.2 to 0.26.

Values of B_{cr}/B_c and M_r/M_s are shown on Day plots [*Day et al*., 1977; *Dunlop*, 2002] to estimate the domain state of the samples (Figure 4a). All of the data fall within the pseudosingle domain (PSD) field. FORC diagrams have closed inner contours centered around 30 mT and some outer contours perpendicular to the vertical axis (B_u) in the region close to the origin of FORC diagrams (Figures 4b–4i), which are indicative of mixtures of single domain (SD) and superparamagnetic (SP) particles [*Roberts et al*., 2000; *Pike et al*., 2001]. Combined with IRM analyses, component 1 should be carried by SD particles, while component 2 is carried by an assemblage of thermally activated (SP) particles. In addition, vertical spreading of FORC distributions along the B_u axis at 40 mT indicates moderate interactions amongst the magnetite particles. These experiments were carried out for pure Al-magnetite without dilution, so magnetic interactions may be enhanced by aggregated particles. The samples were, therefore, diluted in paramagnetic CaF_2 (Figure S3) before measuring hysteresis parameters and FORCs. B_c and M_s are almost stable before and after dilution (Figure S4). Some variations are observed, which may have been caused by the total volume increase of the samples. However, no B_c increase is detected after dilution, which demonstrates that it is not straightforward to separate magnetite particles physically through dilution. FORC diagrams further confirm that magnetic interactions are not reduced by dilution (Figure S5). Thus, when magnetite particles are aggregated due to strong magnetic interactions, it is not easy to separate them at the nanometer scale through physical dilution.

$SIRM_{20\,K}$ warming curves for the Al-magnetite samples are shown in Figure 5. $SIRM_{20\,K}$ for the stoichiometric magnetite samples I-0 and II-0 decreases sharply across the Verwey transition and then decreases slowly to 300 K. However, for magnetite with Al substitution, $SIRM_{20\,K}$ decreases rapidly between 20 K and 50 K, then slowly between 50 K and 80 K, and rapidly again across a broad Verwey transition from 80 K to 120 K. As Al content increases, the Verwey transition becomes broader, and T_v shifts from ~121 K to 96 K for series I samples and from ~120 K to 111 K for series II samples (Figure 5). Once the Al content reaches 16%, the Verwey transition can no longer be detected.

An apparent Verwey transition can also be detected in the $SIRM_{300\,K}$ cycling curves for samples I-0 and II-0, while the Verwey transition becomes less pronounced as Al content increases (Figure 6). In addition, 40–50% of the $SIRM_{300\,K}$ for the pure magnetite samples I-0 and II-0 is demagnetized through cycling between 300 K and 20 K. The magnetic memory (i.e., $SIRM_{300K}$ recovery after warming to room temperature, $SIRM/SIRM_{300K}$) increases with Al substitution from 60% to 95% for series I samples and from 50% to 92% for series II samples. This property could be useful as a proxy for identifying the extent of Al substitution in Al-magnetite.

3.3. Comparison of Magnetite With Different Cation Substitutions

The influence of incorporation of Al and other cations (literature data) on the magnetic properties of magnetite is summarized in Figure 7. B_c values of Series I Al-magnetites increase from 20 to 35 mT until Al content reaches ~2.5% and then decreases to 18 mT with further increasing Al content (left and bottom axes in Figure 7a). In contrast, B_c in the Series II samples increases from 15 to 25 mT with increasing Al content. In addition, $B_{1/2}$ of both components identified from the IRM analysis increases first and then decreases with increasing Al content (Table 2), which demonstrates that Al is incorporated into both components. Co-substituted magnetite samples have a similar B_c trend to Series I samples but with values changing from

10.1002/2016JB012863

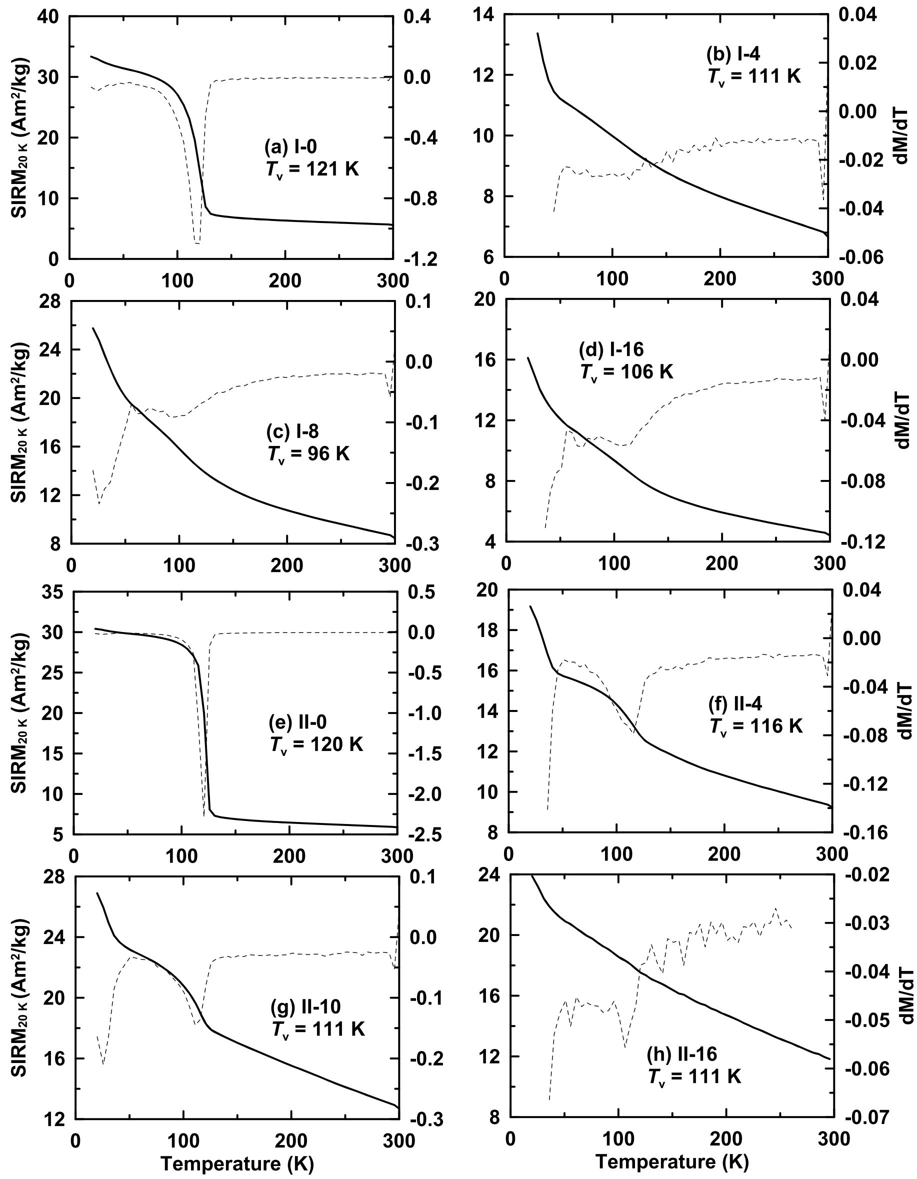

Figure 5. Warming curves of $SIRM_{20\ K}$ produced by a 2.5 T field applied at 20 K after zero-field cooling from 300 to 20 K, where dashed lines represent the first derivative curves of $SIRM_{20\ K}$ with respect to temperature. As Al content increases, the Verwey transition becomes broader, and T_V shifts to lower temperature. Once the Al content reaches 16%, the Verwey transition can no longer be detected.

30 to 125 mT until the Co content reaches 20% and then decreases gradually to 97 mT (right and top axes in Figure 7a). For Zn-substituted magnetite, B_c decreases from 11 to 4 mT as Zn content increases to 17% (left and bottom axes in Figure 7a).

M_s values for our samples decrease from 86 Am^2/kg (series I-0) and 90 Am^2/kg (series II-0) to 19 Am^2/kg (I-16) and 50 Am^2/kg (II-16), respectively, with increasing Al content (Figure 7b). M_s values from literature data for other dopants also decrease with increasing cation doping but with different overall trends. That is, cation incorporation results in reduction of the magnetization of magnetite but to different extents. Additionally, M_s of Zn-magnetite samples is usually larger than that of Al-magnetite for comparable degrees of substitution.

T_c estimates from χ-T curves for Al-magnetite decrease from 580°C to 525°C as Al content increases to 16% (left-hand axis in Figure 7c), so that T_c is higher than that of titanomagnetite with equivalent Ti content

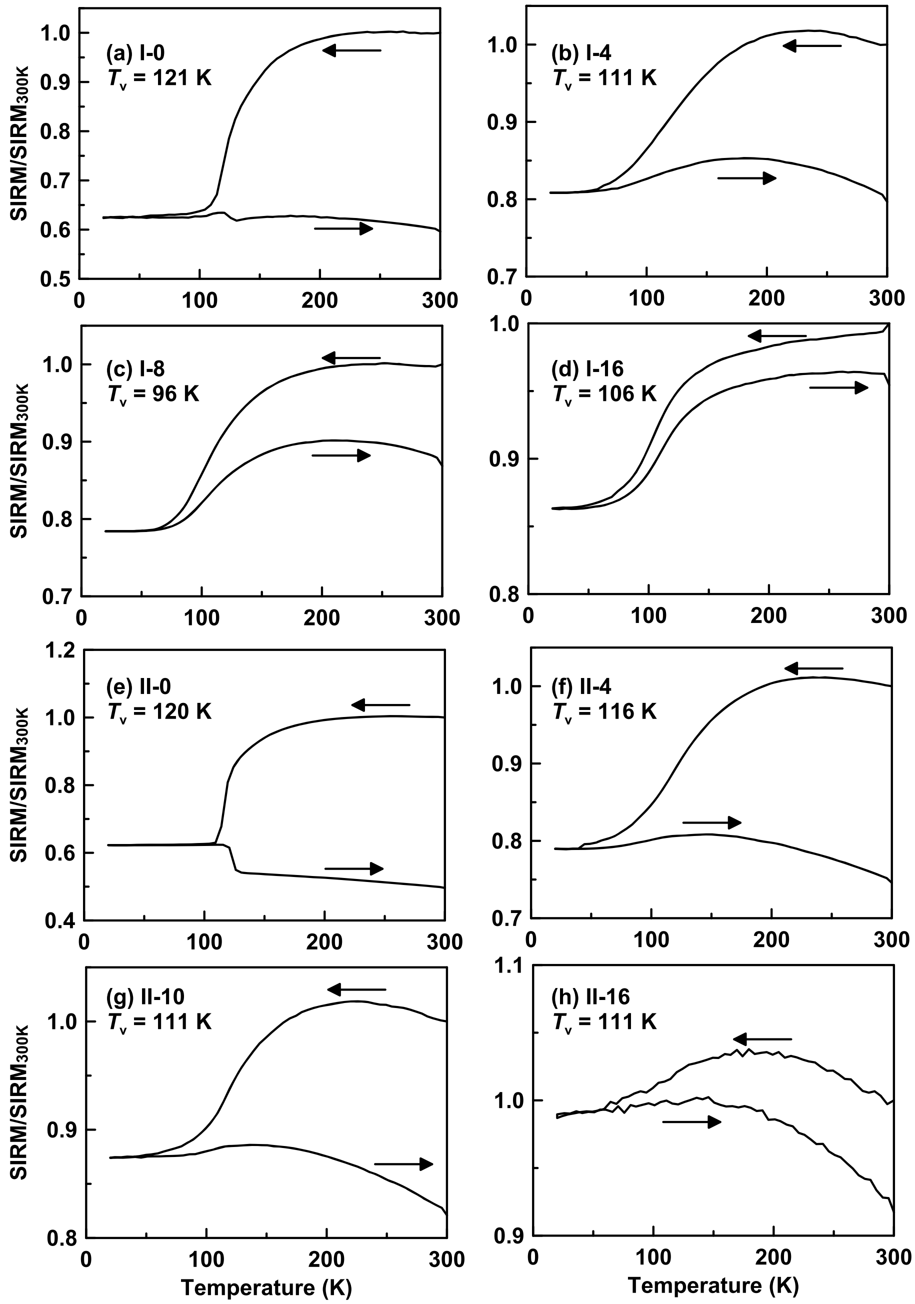

Figure 6. Zero-field cooling and warming curves (300 K → 20 K → 300 K) for $SIRM_{300\ K}$ produced with a 2.5 T field at 300 K. (a–d) Results for series I samples with different Al contents; and for (e–h) series II samples with different Al contents.

(right-hand axis in Figure 7c). In addition, T_v for the Series I samples decreases from 121 K to 96 K as Al content increases to 6.81%, while that of the Series II samples decreases almost linearly from 120 K to 111 K with increasing Al content. Substitution of alternative cations has a more marked effect on T_v compared to the Al substitution in our study (Figure 7d). For example, T_v of titanomagnetite decreases to 85 K when Ti content reaches 3%.

4. Discussion

4.1. Effects of Cation Substitution on the Magnetic Properties of Magnetite

The magnetic effects of substitution of different cation dopants (Ti, Co, Zn, and Ni) for Fe in magnetite have been investigated in a number of studies [*O'Reilly and Banerjee*, 1966; *Readman and O'Reilly*, 1971; *Sidhu et al.*,

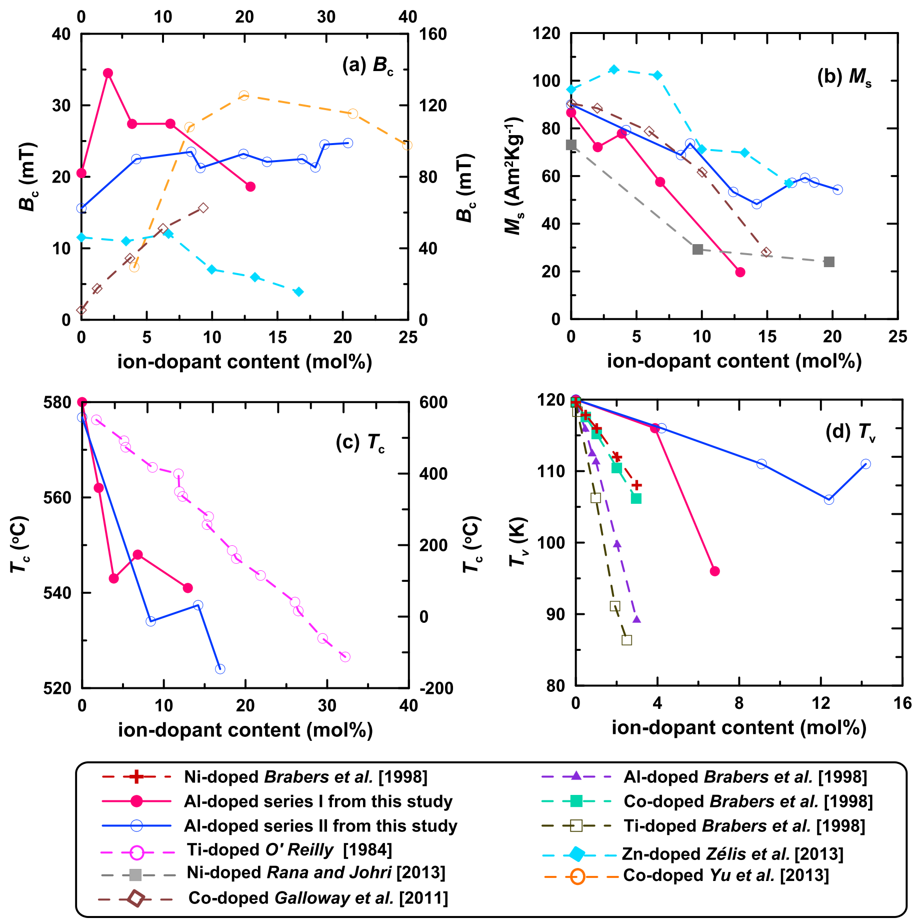

Figure 7. Magnetic parameters versus the content of different cation dopants. (a) Coercivity (B_c) versus cation-dopant content, where the right-hand and upper axes represent Co-doped magnetite and the left-hand and lower axes represent the remaining cases; (b) saturation magnetization (M_s) versus cation-dopant content; (c) Curie temperature (T_c) versus cation-dopant content, where the right-hand axis represents titanomagnetite and the left-hand axis represents Al-doped magnetite; and (d) Verwey transition temperature (T_v) versus cation-dopant content.

1978; *Brabers*, 1995; *Carter-Stiglitz et al.*, 2006; *Varshney and Yogi*, 2010; *Yu et al.*, 2013; *Zélis et al.*, 2013; *Saha et al.*, 2014]. It has been demonstrated that B_c, M_s, T_c, and T_v of magnetite vary systematically with Ti substitution. For example, T_c decreases linearly with increasing Ti content (Figure 7c) [*Day et al.*, 1976, 1977; *Özdemir and O'Reilly*, 1981, 1982; *Moskowitz et al.*, 1998; *Bowles et al.*, 2013]. Based on our study and published data, Al substitution clearly plays a role similar to other cations in controlling the magnetic properties of cation-doped magnetite but with different overall trends (Figure 7). This difference is attributed to differences in the crystallographic sites occupied by different cations.

Magnetite belongs to the cubic crystallographic system and has a spinel structure, with a faced-centered cubic unit cell [*Dunlop and Özdemir*, 1997; *Cornell and Schwertmann*, 2003] that includes both divalent (Fe^{2+}) and trivalent iron (Fe^{3+}). One third of the Fe ions occur as Fe^{3+} on A sites, each of which is surrounded by four O^{2-} anions at the corners of a tetrahedron, while the remaining Fe ions occur as both Fe^{2+} and Fe^{3+} on B sites, each of which is surrounded by six O^{2-} ions at the corner of an octahedron [*O'Reilly*, 1984; *Dunlop and Özdemir*, 1997]. For stoichiometric magnetite, the ratio of Fe^{2+} to Fe^{3+} in the octahedral lattice positions is 0.5. The strong magnetization of magnetite results from the net magnetization of octahedrally coordinated Fe^{2+} on B sites, while the magnetic spin directions of Fe^{3+} on B sites are antiparallel to those on A sites so that they cancel each other completely. In short, the total magnetization is represented by $M_s = M_B - M_A$, where M_B and M_A are the magnetization of the B and A sublattices, respectively.

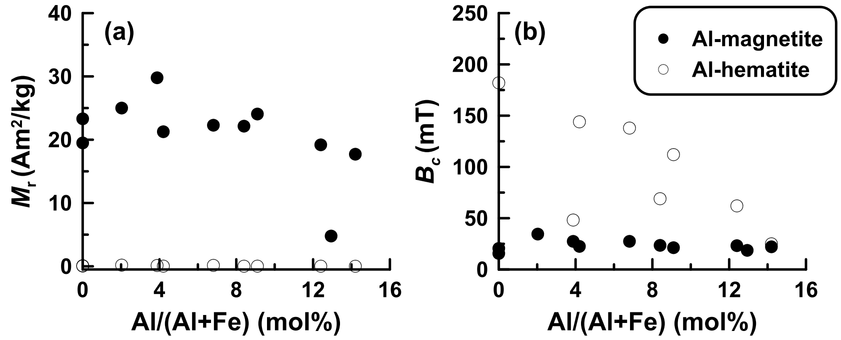

Figure 8. Comparison of results for Al-hematite and Al-magnetite with respect to (a) saturation remanent magnetization (M_r) and (b) coercivity (B_c). Solid and open circles denote Al-magnetite and Al-hematite samples, respectively.

When divalent ions (e.g., Zn^{2+}, Co^{2+}, and Ni^{2+}) are incorporated into magnetite, Fe^{2+} on B sites is preferentially replaced [*Sidhu et al.*, 1978], while Al^{3+} ions are located on both A and B sites but preferentially replace Fe^{3+} on B sites [*Rosenberg et al.*, 1985; *Da Costa et al.*, 1994; *Kozłowski et al.*, 1996]. In contrast, Ti^{4+} substitution not only replaces Fe^{3+} on B sites, but another Fe^{3+} ion must be converted to Fe^{2+} to preserve charge balance ($2Fe^{3+} = Ti^{4+} + Fe^{2+}$), which is fundamentally different from Al^{3+} substitution [*Dunlop and Özdemir*, 1997]. When these ions are incorporated into magnetite, Fe is diluted. Although Co^{2+} and Ni^{2+} are magnetic, they have a net moment of 3 Bohr magnetons (m_b) and 2 m_b, respectively, which is less than that of Fe^{2+} with a net moment of 4 m_b at the high-spin electron state [*Tauxe*, 2010]. Thus, cation substitution decreases M_B more, which gives rise to a lower total M_s for all cation-doped magnetite with increasing substitution (Figure 7b).

For magnetite, B_c is controlled by shape anisotropy, magnetocrystalline anisotropy, internal defects, and magnetic interactions [*Dunlop and Özdemir*, 1997]. TEM results indicate that Al incorporation can influence the long- and short-axis lengths of the Al-magnetite (Figures 1 and 2), which further increases the shape anisotropy (Figure S6). For our two sample series, morphological differences of the particles (platy and quasi-spherical) provide a reason for the different B_c trends. Inclusion of ions into the crystallographic structure is assisted by the flexibility of the oxygen framework, which can expand or contract to accommodate different sized cations [*Cornell and Schwertmann*, 2003]. For example, the smaller Al cation can attract oxygen atoms from neighboring FeO_6-octahedra thereby lengthening the Fe-O bond, which could give rise to substantial lattice distortions and vacancies [*Barrón et al.*, 1984; *Murad and Schwertmann*, 1986]. This process can increase the magnetocrystalline anisotropy and also produce crystal defects, which further increase B_c with respect to stoichiometric magnetite.

Overall, cation substitution will not only weaken the magnetization of magnetite, but it also makes magnetite magnetically harder. Different effects of incorporated cations may be attributed to the diversity of crystallographic sites occupied by these cations. In addition, when substitution distorts the crystal structure, the ordered spins of magnetite become more readily disordered during heating. Therefore, T_c in cation-doped magnetite will decrease with dopant concentration, as it also does in Al-hematite [*Jiang et al.*, 2012].

4.2. Implications of Al-Magnetite for Environmental and Geological Studies

Four factors were proposed by *Mullins* [1977] to give rise to magnetic enhancement of upper soil layers, including fermentation, biogenic contributions, burning, and atmospheric fallout of magnetic spherules. Fermentation, which is one kind of pedogenesis, is the most significant pathway for magnetite formation in the upper layers, where magnetite or maghemite formation results from reduction or oxidation of poorly crystalline iron oxides [*Maher*, 1998]. In addition, lithogenic magnetite has a relatively high stability and is indispensible for soil magnetic enhancement [*Fine et al.*, 1995; *Vidic et al.*, 2000]. Due to the widespread significance of fire, burning is also an undoubted factor for magnetic enhancement [*Mullins*, 1977; *Maher*, 1986, 1998], as proposed by *Le Borgne* [1955]. Under the action of reducing gases such as CO produced by organic matter combustion, weakly magnetic minerals (e.g., hematite) can be reduced to magnetite, which leads to enhancement of magnetic susceptibility and SIRM [*Mullins*, 1977; *Blake et al.*, 2006; *Oldfield and Crowther*, 2007]. As shown in Figure 8, M_r increases from ~0.04 Am^2/kg to ~25 Am^2/kg for samples before (hematite) and after heating (magnetite), while B_c decreases from ~180 mT to 20 mT. These data provide direct evidence for magnetic enhancement in natural environments because of high-temperature mineral transformation. However, the resulting enhancement level depends on soil-specific factors, such as the concentrations of reductants (e.g., organic matter) and iron, soil porosity, and temperature [*Oldfield et al*., 1981; *Maher*, 1986]. Clay minerals can also reduce hematite to magnetite during heating so that magnetic enhancement is controlled by clay mineral content and iron concentration [*Zhang et al*., 2012; *Jiang et al*., 2015]. Moreover, in the presence of iron-reducing bacteria and organic matter, weakly magnetic high-coercivity minerals in well-drained soils can be transformed to strongly magnetic low-coercivity ferrimagnetic minerals [*Oldfield*, 1992, 2007; *Nie et al*., 2010]. *Bloemendal and Liu* [2005] reported the selective destruction of hematite within the uppermost part of paleosol S5 at the Luochuan section on the Chinese Loess Plateau. They found that the highest SIRM and χ values in S5 coincided with the minimum hard IRM (HIRM) value, which suggests the reduction of hematite to magnetite. In contrast, if a soil is waterlogged, hematite will not be reduced to magnetite, but instead both minerals will dissolve reductively, which results in an overall loss of magnetization [*Maher*, 1998; *Guo et al*., 2001; *Hu et al*., 2013; *Roberts*, 2015].

We have found that magnetite formed by reduction of hematite during heating retains distinctive characteristics of the parent hematite. The Series I magnetite samples have micropores on their surfaces, which can be attributed to the release of structural water and crystal distortion during heating and dehydration. *Pomies et al*. [1999] also observed micropores in hematite surfaces that arose from goethite dehydration at high temperature. In addition, micropores have been detected on the surfaces of magnetite produced by reduction of hematite ore at high temperature [*Swann and Tighe*, 1977]. *Wolska* [1981] proposed that most of the hematite produced in aqueous systems contains some structural OH and/or H_2O combined with Fe vacancies, which could be removed by high-temperature heating [*Schwertmann et al*., 1999; *Schwertmann and Cornell*, 2000]. No micropores are observed on the surface of the Series II samples, however, because the parent hematite was produced at high temperature and no water remained in the hematite structure. We, therefore, suggest that micropores on the surface of magnetite particles can be used as a signature of transformation from hematite that formed at low temperature and that was subsequently dehydrated at elevated temperatures to form Al-magnetite. These surface micropores could provide a potential fingerprint of soil burning.

It has been proposed that lithogenic magnetite usually does not contain Al to any significant extent [*Schwertmann and Murad*, 1990]. Thus, the occurrence of Al-magnetite in nature is attributed to the conversion of Al-goethite or Al-hematite via heating under reducing conditions [*Schwertmann and Fechter*, 1984]. *Schwertmann and Murad* [1990] synthesized Al-magnetite directly from solution at ambient temperatures but with Al content less than 3 mol%. Therefore, it is reasonable to expect magnetite with significant Al substitution to have been produced from Al-goethite or Al-hematite and that its presence in natural environments can be used as an indicator of reducing high-temperature environments. For example, magnetic enhancement is prevalent in fault gouge [*Hirono et al*., 2006; *Mishima et al*., 2009; *Yang et al*., 2012], which is interpreted as resulting from decomposition of clay minerals or other iron oxides (e.g., siderite or lepidocrocite) driven by frictional heating during earthquake fault rupture [*Ferré et al*., 2005; *Fukuchi et al*., 2005; *Chou et al*., 2012; *Yang et al*., 2012]. A mineral with T_c of ~560°C has been detected in χ-T curves for magnetically enhanced fault gouge samples. Based on our results, this mineral could be cation-substituted magnetite produced by reduction of cation-doped hematite driven by shear friction heating.

In addition, Al-magnetite is misinterpreted occasionally as titanomagnetite in magnetic studies of soils. For example, T_c values below 580°C are often used to indicate the presence of titanomagnetite in natural samples, especially in igneous rocks [*Qin et al*., 2011] and archeological samples [*Mitra et al*., 2013]. However, as indicated in Figure 7, Al substitution also lowers T_c significantly in magnetite. In addition, magnetic minerals with T_c just below 580°C are prevalent in the cooling segments of χ-T curves for soils [*Liu et al*., 2005, 2010] and sediments [*Li et al*., 2013], which may result from the formation of Al-magnetite from Al-hematite during the heating portion of the χ-T experiment [*Zhang et al*., 2012; *Jiang et al*., 2015]. Therefore, discrimination of titanomagnetite from Al-magnetite is of considerable practical importance in mineral magnetism.

Based on data from previous studies of titanomagnetite and our results (Figure 9), it can be seen that compared with Ti, Al substitution has a subtler effect on the magnetic properties of magnetite. The T_c of Al-magnetite varies in the 520–580°C range, while that of Ti-rich titanomagnetite can be as low as −150°C

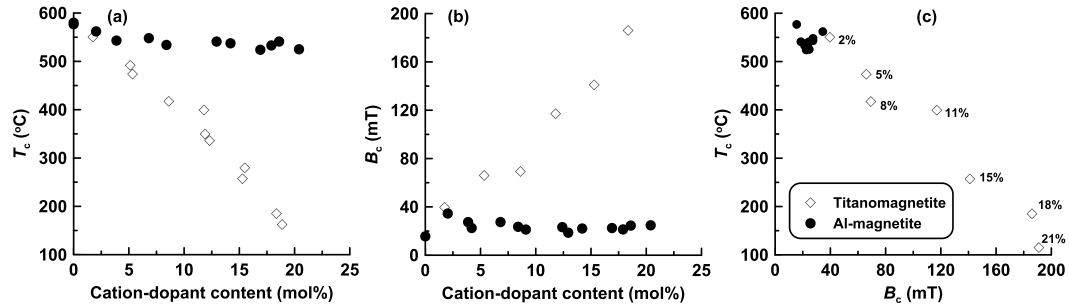

Figure 9. Comparison of results for titanomagnetite and Al-magnetite for (a) T_C versus cation-dopant content, where the titanomagnetite data are from *O'Reilly* [1984]; (b) B_C versus ion-dopant content, where the titanomagnetite data are from *Day et al*. [1976, 1977]; and (c) correlation of T_C versus B_C, where the numbers represent Al or Ti content.

[*O'Reilly*, 1984] when Ti concentration exceeds 30 mol% (Figure 9a). Additionally, B_c of Al-magnetite varies around 20 mT, while that of Ti-rich titanomagnetite varies up to 200 mT (Figure 9b). For samples with similar T_c, titanomagnetite clearly has higher coercivities than Al-magnetite. Al-magnetite and titanomagnetite have distinct data distributions in a plot of T_c versus B_c (Figure 9c). Al-magnetite data cluster, while those for titanomagnetite follow a linear trend with increasing Ti concentration. The correlation of T_c and B_c for titanomagnetite can be used to help discriminate titanomagnetite from Al-magnetite. However, more definitive identification is likely to require a combination of multiple methods. In soils, titanomagnetite is a common product of physical weathering of igneous rocks (e.g., tephra or basalts) [*Morris et al*., 1990; *De Oliveira et al*., 2002], while Al-magnetite forms mainly through secondary pedogenic processes and records more information about the soil-forming environment [*Schwertmann and Murad*, 1990], which may lead to different particle morphologies. Therefore, morphological characteristics and elemental analysis can be determined using scanning electron microscopy and energy dispersive spectrometry to distinguish these two kinds of minerals. Discrimination between these two minerals will be important for environmental and climatic studies.

5. Conclusions

Al substitution greatly affects the magnetic properties of Al-magnetite. For example, B_c increases with increasing Al content and then decreases slightly, while M_s, T_c, and T_v all decrease with increasing Al content. Our Al-magnetite samples inherited morphological features of the original Al-hematite from which they were transformed, with the formation of surficial micropores in the Series I samples resulting from the release of structural water. This feature could be used as a fingerprint of natural soil burning. Moreover, different T_c and B_c trends can be used to discriminate titanomagnetite from Al-magnetite, which should be useful for magnetic mineral identification in environmental magnetic studies.

Acknowledgments
We thank Congcong Gai for helping during measurements. This study was supported by National Program on Global Change and Air-Sea Interaction (GASI-04-01-02), the National Natural Science Foundation of China (grants 41504055, 41430962, 41374073, and 41025013), and Chinese Continental Shelf Deep Drilling Program (GZH201100202). Z.X.J. further acknowledges support from the China Postdoctoral Science Foundation. A.P.R. and D.H. acknowledge support from the Australian Research Council (grants DP110105419 and DP120103952). Relevant data for this paper are available in Tables 1 and 2.

References

Akimoto, S., T. Nagata, and T. Katsura (1957), The $TiFe_2O_5$-Ti_2FeO_5 solid solution series, *Nature*, *179*, 37–38.

Allan, J. E., J. Coey, I. Sanders, U. Schwertmann, G. Friedrich, and A. Wiechowski (1989), An occurrence of a fully-oxidized natural titanomaghemite in basalt, *Mineral. Mag.*, *53*, 299–304.

Bailey, I., Q. Liu, G. E. A. Swann, Z. Jiang, Y. Sun, X. Zhao, and A. P. Roberts (2011), Iron fertilisation and biogeochemical cycles in the sub-Arctic northwest Pacific during the late Pliocene intensification of Northern Hemisphere glaciation, *Earth Planet. Sci. Lett.*, *307*, 253–265.

Barrón, V., J. Rendón, J. Torrent, and C. Serna (1984), Relation of infrared, crystallochemical, and morphological properties of Al-substituted hematites, *Clays Clay Miner.*, *32*, 475–479.

Blake, W., P. Wallbrink, S. Doerr, R. Shakesby, and G. Humphreys (2006), Magnetic enhancement in wildfire-affected soil and its potential for sediment-source ascription, *Earth Surf. Processes Landforms*, *31*, 249–264.

Blakemore, R., K. Short, D. A. Bazylinski, C. Rosenblatt, and R. B. Frankel (1985), Microaerobic conditions are required for magnetite formation within *Aquaspirillum magnetotacticum*, *Geomicrobiol. J.*, *4*, 53–71.

Bleil, U., and N. Petersen (1983), Variations in magnetization intensity and low-temperature titanomagnetite oxidation of ocean floor basalts, *Nature*, *301*, 384–388.

Bloemendal, J., and X. Liu (2005), Rock magnetism and geochemistry of two Plio-Pleistocene Chinese loess-palaeosol sequences—Implications for quantitative palaeoprecipitation reconstruction, *Palaeogeogr. Palaeoclimatol. Palaeoecol.*, *226*, 149–166.

Bowles, J. A., M. J. Jackson, T. S. Berquó, P. A. Sølheid, and J. S. Gee (2013), Inferred time and temperature-dependent cation ordering in natural titanomagnetites, *Nat. Commun.*, *4*, 1–9.

Brabers, V. (1995), The electrical conduction of titanomagnetites, *Physica B*, *205*, 143–152.

Brabers, V., and J. Hendrinks (1982), Magnetostriction of aluminium substituted magnetite, *J. Magn. Magn. Mater.*, *26*, 300–302.
Brabers, V., F. Walz, and H. Kronmüller (1998), Impurity effects upon the Verwey transition in magnetite, *Phys. Rev. B*, *58*, 14,163–14,166.
Carter-Stiglitz, B., B. Moskowitz, P. Solheid, T. S. Berquó, M. Jackson, and A. Kosterov (2006), Low-temperature magnetic behavior of multidomain titanomagnetites: TM0, TM16, and TM35, *J. Geophys. Res.*, *111*, B12S05, doi:10.1029/2006JB004561.
Chou, Y.-M., S.-R. Song, C. Aubourg, Y.-F. Song, A.-M. Boullier, T.-Q. Lee, M. Evans, E.-C. Yeh, and Y.-M. Chen (2012), Pyrite alteration and neoformed magnetic minerals in the fault zone of the Chi-Chi earthquake (M_w7.6, 1999): Evidence for frictional heating and co-seismic fluids, *Geochem. Geophys. Geosyst.*, *13*, Q08002, doi:10.1029/2012GC004120.
Cornell, R., and U. Schwertmann (2003), *The Iron Oxides*, Weinheim, VCH.
Da Costa, A. C. S. D., J. M. Bigham, F. E. Rhoton, and S. J. Traina (1999), Quantification and characterization of maghemite in soils derived from volcanic rocks in southern Brazil, *Clays Clay Miner.*, *47*, 466–473.
Da Costa, G., E. De Grave, A. Bryan, and L. Bowen (1994), Mössbauer studies of nano-sized aluminum-substituted maghemites, *Hyperfine Interact.*, *94*, 1983–1987.
Day, R., M. Fuller, and V. Schmidt (1976), Magnetic hysteresis properties of synthetic titanomagnetites, *J. Geophys. Res.*, *81*, 873–880, doi:10.1029/JB081i005p00873.
Day, R., M. Fuller, and V. A. Schmidt (1977), Hysteresis properties of titanomagnetites: Grain-size and compositional dependence, *Phys. Earth Planet. Inter.*, *13*, 260–267.
De Oliveira, M. T. G., M. L. Formoso, M. I. da Costa, and A. Meunier (2002), The titanomagnetite to titanomaghemite conversion in a weathered basalt profile from southern Parana Basin, Brazil, *Clays Clay Miner.*, *50*, 478–493.
De Boer, C. B., M. J. Dekkers, and T. A. M. van Hoof (2001), Rock-magnetic properties of TRM carrying baked and molten rocks straddling burnt coal seams, *Phys. Earth Planet. Inter.*, *126*, 93–108.
Dearing, J., P. Bird, R. Dann, and S. Benjamin (1997), Secondary ferrimagnetic minerals in Welsh soils: A comparison of mineral magnetic detection methods and implications for mineral formation, *Geophys. J. Int.*, *130*, 727–736.
Duce, R., C. Unni, B. Ray, J. Prospero, and J. Merrill (1980), Long-range atmospheric transport of soil dust from Asia to the tropical North Pacific: Temporal variability, *Science*, *209*, 1522–1524.
Dunlop, D. J. (2002), Theory and application of the Day plot (M_{rs}/M_s versus H_{cr}/H_c) 1. Theoretical curves and tests using titanomagnetite data, *J. Geophys. Res.*, *107*(B3), 2056, doi:10.1029/2001JB000486.
Dunlop, D. J., and Ö. Özdemir (1997), *Rock Magnetism: Fundamentals and Frontiers*, Cambridge Univ. Press, Cambridge.
Egli, R. (2004), Characterization of individual rock magnetic components by analysis of remanence curves: 2. Fundamental properties of coercivity distributions, *Phys. Chem. Earth*, *29*, 851–867.
Enomoto, Y., and Z. Zheng (1998), Possible evidences of earthquake lightning accompanying the 1995 Kobe earthquake inferred from the Nojima fault gouge, *Geophys. Res. Lett.*, *25*, 2721–2724, doi:10.1029/98GL02015.
Evans, M. E., and F. Heller (2003), *Environmental Magnetism: Principles and Applications of Enviromagnetics*, Academic Press, San Diego, Calif.
Ferré, E., M. Zechmeister, J. Geissman, N. Mathana Sekaran, and K. Kocak (2005), The origin of high magnetic remanence in fault pseudotachylites: Theoretical considerations and implication for coseismic electrical currents, *Tectonophysics*, *402*, 125–139.
Fine, P., K. L. Verosub, and M. J. Singer (1995), Pedogenic and lithogenic contributions to the magnetic susceptibility record of the Chinese loess/palaeosol sequence, *Geophys. J. Int.*, *122*, 97–107.
Fukuchi, T., K. Mizoguchi, and T. Shimamoto (2005), Ferrimagnetic resonance signal produced by frictional heating: A new indicator of paleoseismicity, *J. Geophys. Res.*, *110*, B12404, doi:10.1029/2004JB003485.
Galloway, J. M., A. Arakaki, F. Masuda, T. Tanaka, T. Matsunaga, and S. S. Staniland (2011), Magnetic bacterial protein Mms6 controls morphology, crystallinity and magnetism of cobalt-doped magnetite nanoparticles *in vitro*, *J. Mater. Chem.*, *21*, 15,244–15,254.
Gedye, S., R. Jones, W. Tinner, B. Ammann, and F. Oldfield (2000), The use of mineral magnetism in the reconstruction of fire history: A case study from Lago di Origlio, Swiss Alps, *Palaeogeogr. Palaeoclimatol. Palaeoecol.*, *164*, 101–110.
Geiss, C. E., and C. W. Zanner (2006), How abundant is pedogenic magnetite? Abundance and grain size estimates for loessic soils based on rock magnetic analyses, *J. Geophys. Res.*, *111*, B12S21, doi:10.1029/2006JB004564.
Geiss, C. E., R. Egli, and C. W. Zanner (2008), Direct estimates of pedogenic magnetite as a tool to reconstruct past climates from buried soils, *J. Geophys. Res.*, *113*, B11102, doi:10.1029/2008JB005669.
Gibbs-Eggar, Z., B. Jude, J. Dominik, J.-L. Loizeau, and F. Oldfield (1999), Possible evidence for dissimilatory bacterial magnetite dominating the magnetic properties of recent lake sediments, *Earth Planet. Sci. Lett.*, *168*, 1–6.
Glasby, G. (1991), Mineralogy, geochemistry, and origin of Pacific red clays: A review, *N. Z. J. Geol. Geophys.*, *34*, 167–176.
Goulart, A., J. Fabris, M. de Jesus Filho, J. Coey, G. da Costa, and E. de Grave (1998), Iron oxides in a soil developed from basalt, *Clays Clay Miner.*, *46*, 369–378.
Guo, Z., S. Peng, Q. Hao, P. Biscaye, and T. Liu (2001), Origin of the Miocene–Pliocene red-earth formation at Xifeng in Northern China and implications for paleoenvironments, *Palaeogeogr. Palaeoclimatol. Palaeoecol.*, *170*, 11–26.
Guyodo, Y., T. M. LaPara, A. J. Anschutz, R. L. Penn, S. K. Banerjee, C. E. Geiss, and W. Zanner (2006), Rock magnetic, chemical and bacterial community analysis of a modern soil from Nebraska, *Earth Planet. Sci. Lett.*, *251*, 168–178.
Haliuc, A., S. M. Hutchinson, G. Florescu, and A. Feurdean (2016), The role of fire in landscape dynamics: An example of two sediment records from the Rodna Mountains, northern Romanian Carpathians, *Catena*, *137*, 432–440.
Han, R., T. Shimamoto, J. I. Ando, and J. H. Ree (2007), Seismic slip record in carbonate-bearing fault zones: An insight from high-velocity friction experiments on siderite gouge, *Geology*, *35*, 1131–1134.
Hanesch, M., H. Stanjek, and N. Petersen (2006), Thermomagnetic measurements of soil iron minerals: The role of organic carbon, *Geophys. J. Int.*, *165*, 53–61.
Heslop, D., M. Dekkers, P. Kruiver, and I. Van Oorschot (2002), Analysis of isothermal remanent magnetization acquisition curves using the expectation maximization algorithm, *Geophys. J. Int.*, *148*, 58–64.
Heslop, D., G. McIntosh, and M. Dekkers (2004), Using time- and temperature-dependent Preisach models to investigate the limitations of modelling isothermal remanent magnetization acquisition curves with cumulative log Gaussian functions, *Geophys. J. Int.*, *157*, 55–63.
Hirono, T., W. Lin, E. C. Yeh, W. Soh, Y. Hashimoto, H. Sone, O. Matsubayashi, K. Aoike, H. Ito, and M. Kinoshita (2006), High magnetic susceptibility of fault gouge within Taiwan Chelungpu fault: Nondestructive continuous measurements of physical and chemical properties in fault rocks recovered from Hole B, TCDP, *Geophys. Res. Lett.*, *33*, L15303, doi:10.1029/2006GL026133.
Hu, P., Q. Liu, J. Torrent, V. Barrón, and C. Jin (2013), Characterizing and quantifying iron oxides in Chinese loess/paleosols: Implications for pedogenesis, *Earth Planet. Sci. Lett.*, *369–370*, 271–283.
Jiang, Z., Q. Liu, V. Barrón, J. Torrent, and Y. Yu (2012), Magnetic discrimination between Al-substituted hematites synthesized by hydrothermal and thermal dehydration methods and its geological significance, *J. Geophys. Res.*, *117*, B02102, doi:10.1029/2011JB008605.

Jiang, Z., Q. Liu, M. J. Dekkers, C. Colombo, Y. Yu, V. Barrón, and J. Torrent (2014), Ferro and antiferromagnetism of ultrafine-grained hematite, *Geochem. Geophys. Geosyst.*, *15*, 2699–2712, doi:10.1002/2014GC005377.

Jiang, Z., Q. Liu, X. Zhao, C. Jin, C. Liu, and S. Li (2015), Thermal magnetic behaviour of Al-substituted haematite mixed with clay minerals and its geological significance, *Geophys. J. Int.*, *200*, 130–143.

Kletetschka, G., and S. K. Banerjee (1995), Magnetic stratigraphy of Chinese loess as a record of natural fires, *Geophys. Res. Lett.*, *22*, 1341–1343, doi:10.1029/95GL01324.

Kozłowski, A., P. Metcalf, Z. Kąkol, and J. Honig (1996), Electrical and magnetic properties of Fe_{3-z} Al_zO_4 ($z < 0.06$), *Phys. Rev. B*, *53*, 15,113–15,118.

Kruiver, P. P., M. J. Dekkers, and D. Heslop (2001), Quantification of magnetic coercivity components by the analysis of acquisition curves of isothermal remanent magnetisation, *Earth Planet. Sci. Lett.*, *189*, 269–276.

Le Borgne, E. (1955), Abnormal magnetic susceptibility of the top soil, *Ann. Geophys.*, *11*, 399–419.

Li, S., C. Deng, H. Yao, S. Huang, C. Liu, H. He, Y. Pan, and R. Zhu (2013), Magnetostratigraphy of the Dali Basin in Yunnan and implications for late Neogene rotation of the southeast margin of the Tibetan Plateau, *J. Geophys. Res. Solid Earth*, *118*, 791–807, doi:10.1002/jgrb.50129.

Liu, C. C., C. Deng, Q. Liu, L. Zheng, W. Wang, X. Xu, S. Huang, and B. Yuan (2010), Mineral magnetism to probe into the nature of palaeomagnetic signals of subtropical red soil sequences in southern China, *Geophys. J. Int.*, *181*, 1395–1410.

Liu, Q., C. Deng, Y. Yu, J. Torrent, M. Jackson, S. Banerjee, and R. Zhu (2005), Temperature dependence of magnetic susceptibility in an argon environment: Implications for pedogenesis of Chinese loess/palaeosols, *Geophys. J. Int.*, *161*, 102–112.

Lovley, D. R., J. F. Stolz, G. L. Nord, and E. J. Phillips (1987), Anaerobic production of magnetite by a dissimilatory iron-reducing microorganism, *Nature*, *330*, 252–254.

Maher, B. (1986), Characterisation of soils by mineral magnetic measurements, *Phys. Earth Planet. Inter.*, *42*, 76–92.

Maher, B. (1998), Magnetic properties of modern soils and Quaternary loessic paleosols: Paleoclimatic implications, *Palaeogeogr. Palaeoclimatol. Palaeoecol.*, *137*, 25–54.

Maher, B., and R. M. Taylor (1989), Formation of ultrafine-grained magnetite in soils, *Nature*, *336*, 368–370.

Mishima, T., T. Hirono, N. Nakamura, W. Tanikawa, W. Soh, and S. R. Song (2009), Changes to magnetic minerals caused by frictional heating during the 1999 Taiwan Chi-Chi earthquake, *Earth Planets Space*, *61*, 797–801.

Mitra, R., L. Tauxe, and S. K. McIntosh (2013), Two thousand years of archeointensity from West Africa, *Earth Planet. Sci. Lett.*, *364*, 123–133.

Morris, R. V., J. L. Gooding, H. V. Lauer, and R. B. Singer (1990), Origins of Mars-like spectral and magnetic properties of a Hawaiian palagonitic soil, *J. Geophys. Res.*, *95*, 14,427–14,434, doi:10.1029/JB095iB09p14427.

Moskowitz, B. M., M. Jackson, and C. Kissel (1998), Low-temperature magnetic behavior of titanomagnetites, *Earth Planet. Sci. Lett.*, *157*, 141–149.

Mullins, C. (1977), Magnetic susceptibility of the soil and its significance in soil science—A review, *J. Soil Sci.*, *28*, 223–246.

Murad, E., and U. Schwertmann (1986), Influence of A1 substitution and crystal size on the room-temperature Mössbauer spectrum of hematite, *Clays Clay Miner.*, *34*, 1–6.

Nagata, T. (1962), Magnetic properties of ferrimagnetic minerals of Fe-Ti-O system, in *Proc. Benedum Earth Magnetism Symp*, pp. 69–86, Univ. of Pittsburgh Press, Pittsburgh, Pa.

Nie, J., Y. Song, J. W. King, X. Fang, and C. Heil (2010), HIRM variations in the Chinese red-clay sequence: Insights into pedogenesis in the dust source area, *J. Asian Earth Sci.*, *38*, 96–104.

Oldfield, F., R. Thompson, and D. Dickson (1981), Artificial magnetic enhancement of stream bedload: A hydrological application of superparamagnetism. *Phys. Earth Planet. Inter.*, *26*, 107–124.

Oldfield, F. (1992), The source of fine-grained 'magnetite' in sediments, *Holocene*, *2*, 180–182.

Oldfield, F. (2007), Sources of fine-grained magnetic minerals in sediments: A problem revisited, *Holocene*, *17*, 1265–1271.

Oldfield, F., and J. Crowther (2007), Establishing fire incidence in temperate soils using magnetic measurements, *Palaeogeogr. Palaeoclimatol. Palaeoecol.*, *249*, 362–369.

Oliva-Urcia, B., A. Kontny, C. Vahle, and A. M. Schleicher (2011), Modification of the magnetic mineralogy in basalts due to fluid-rock interactions in a high-temperature geothermal system (Krafla, Iceland), *Geophys. J. Int.*, *186*, 155–174.

O'Reilly, W. (1984), *Rock and Mineral Magnetism*, Blackie, Glasgow.

O'Reilly, W., and S. Banerjee (1966), Oxidation of titanomagnetites and self-reversal, *Nature*, *211*, 26–28.

Ortega, B., M. Caballero, S. Lozano, G. Vilaclara, and A. Rodríguez (2006), Rock magnetic and geochemical proxies for iron mineral diagenesis in a tropical lake: Lago Verde, Los Tuxtlas, East-Central Mexico, *Earth Planet. Sci. Lett.*, *250*, 444–458.

Özdemir, Ö., and D. J. Dunlop (2010), Hallmarks of maghemitization in low-temperature remanence cycling of partially oxidized magnetite nanoparticles, *J. Geophys. Res.*, *115*, B02101, doi:10.1029/2009JB006756.

Özdemir, Ö., and W. O'Reilly (1981), High-temperature hysteresis and other magnetic properties of synthetic monodomain titanomagnetites, *Phys. Earth Planet. Inter.*, *25*, 406–418.

Özdemir, Ö., and W. O'Reilly (1982), Magnetic hysteresis properties of synthetic monodomain titanomaghemites, *Earth Planet. Sci. Lett.*, *57*, 437–447.

Pan, Y. X., Q. Liu, C. Deng, H. F. Qin, and R. X. Zhu (2006), Thermally induced inversion of Al-substituted titanomagnetite in basalts: Evidence for partial self-reversal, *J. Geophys. Res.*, *111*, B12S29, doi:10.1029/2006JB004576.

Petrovský, E., and A. Kapička (2006), On determination of the Curie point from thermomagnetic curves, *J. Geophys. Res.*, *111*, B12S27, doi:10.1029/2006JB004507.

Pike, C. R., A. P. Roberts, and K. L. Verosub (2001), First-order reversal curve diagrams and thermal relaxation effects in magnetic particles, *Geophys. J. Int.*, *145*, 721–730.

Pomies, M., M. Menu, and C. Vignaud (1999), TEM observations of goethite dehydration: Application to archaeological samples, *J. Eur. Ceram. Soc.*, *19*, 1605–1614.

Prospero, J. M., P. Ginoux, O. Torres, S. E. Nicholson, and T. E. Gill (2002), Environmental characterization of global sources of atmospheric soil dust identified with the Nimbus 7 Total Ozone Mapping Spectrometer (TOMS) absorbing aerosol product, *Rev. Geophys.*, *40*(1), 1002, doi:10.1029/2000RG000095.

Qin, H., H. He, Q. Liu, and S. Cai (2011), Palaeointensity just at the onset of the Cretaceous normal superchron, *Phys. Earth Planet. Inter.*, *187*, 199–211.

Rana, G., and U. C. Johri (2013), A study on structural and magnetic properties of Ni-substituted magnetite nanoparticles, *J. Alloys Compd.*, *577*, 376–381.

Readman, P., and W. O'Reilly (1971), The synthesis and inversion of non-stoichiometric titanomagnetites, *Phys. Earth Planet. Inter.*, *4*, 121–128.

Roberts, A. P. (2015), Magnetic mineral diagenesis, *Earth Sci. Rev.*, *151*, 1–47.

Roberts, A. P., C. R. Pike, and K. L. Verosub (2000), First-order reversal curve diagrams: A new tool for characterizing the magnetic properties of natural samples, *J. Geophys. Res.*, *105*, 28,461–28,475, doi:10.1029/2000JB900326.

Roberts, A. P., L. Chang, D. Heslop, F. Florindo, and J. C. Larrasoaña (2012), Searching for single domain magnetite in the “pseudo-single-domain” sedimentary haystack: Implications of biogenic magnetite preservation for sediment magnetism and relative paleointensity determinations, *J. Geophys. Res.*, *117*, B08104, doi:10.1029/2012JB009412.

Roberts, A. P., F. Florindo, L. Chang, D. Heslop, L. Jovane, and J. C. Larrasoaña (2013), Magnetic properties of pelagic marine carbonates, *Earth Sci. Rev.*, *127*, 111–139.

Rosenberg, M., P. Deppe, H. Janssen, V. Brabers, F. Li, and S. Dey (1985), A Mössbauer study of Al and Ga substituted magnetite, *J. Appl. Phys.*, *57*, 3740–3742.

Saha, D. R., A. K. Nandi, and D. Chakravorty (2014), Exchange bias effect in composites of CuO nanoparticles and nanosilica glass, *J. Magn. Magn. Mater.*, *355*, 184–187.

Scholz, C. H. (2002), *The Mechanics of Earthquakes and Faulting*, Cambridge Univ. Press, Cambridge.

Schwertmann, U. (1988), Occurrence and formation of iron oxides in various pedoenvironments, in *Iron in Soils and Clay Minerals*, edited by J. W. Stucki et al., pp. 267–308, Reidel, Amsterdam.

Schwertmann, U., and R. M. Cornell (2000), *Iron Oxides in the Laboratory*, Wiley-VCH, Weinheim.

Schwertmann, U., and H. Fechter (1984), The influence of aluminum on iron oxides: XI. Aluminum-substituted maghemite in soils and its formation, *Soil Sci. Soc. Am. J.*, *48*, 1462–1463.

Schwertmann, U., and E. Murad (1990), The influence of aluminum on iron oxides: XIV. Al-substituted magnetite synthesized at ambient temperatures, *Clays Clay Miner.*, *38*, 196–202.

Schwertmann, U., R. W. Fitzpatrick, and J. Le Roux (1977), Al substitution and different disorder in soil hematites, *Clays Clay Miner.*, *25*, 373–374.

Schwertmann, U., J. Friedl, and H. Stanjek (1999), From Fe (III) ions to ferrihydrite and then to hematite, *J. Colloid Interface Sci.*, *209*, 215–223.

Sidhu, P., R. Gilkes, and A. Posner (1978), The synthesis and some properties of Co, Ni, Zn, Cu, Mn and Cd substituted magnetites, *J. Inorg. Nucl. Chem.*, *40*, 429–435.

Snowball, I. F. (1994), Bacterial magnetite and the magnetic properties of sediments in a Swedish lake, *Earth Planet. Sci. Lett.*, *126*, 129–142.

Swann, P., and N. Tighe (1977), High voltage microscopy of the reduction of hematite to magnetite, *Metall. Mater. Trans. B*, *8*, 479–487.

Tanikawa, W., T. Mishima, T. Hirono, W. Lin, T. Shimamoto, W. Soh, and S. R. Song (2007), High magnetic susceptibility produced in high-velocity frictional tests on core samples from the Chelungpu fault in Taiwan, *Geophys. Res. Lett.*, *34*, L15304, doi:10.1029/2007GL030783.

Tanikawa, W., T. Mishima, T. Hirono, W. Soh, and S. R. Song (2008), High magnetic susceptibility produced by thermal decomposition of core samples from the Chelungpu fault in Taiwan, *Earth Planet. Sci. Lett.*, *272*, 372–381.

Tauxe, L. (2010), *Essentials of Paleomagnetism*, Univ. of Calif. Press, Berkeley.

Taylor, R. (1987), Magnetite in soils: I. The synthesis of single-domain and superparamagnetic magnetite, *Clay Miner.*, *22*, 411–422.

Tite, M. S., and C. Mullins (1971), Enhancement of the magnetic susceptibility of soils on archaeological sites, *Archaeometry*, *13*, 209–219.

Tunstall, B. R., T. Martin, J. Walker, A. Gill, and A. Aston (1976), *Soil Temperatures Induced by an Experimental Log Pile Fire: Preliminary Data Analysis*, CSIRO, Division of Land Use Research, Canberra.

Varshney, D., and A. Yogi (2010), Structural and transport properties of stoichiometric and Cu^{2+}-doped magnetite: $Fe_{3-x}Cu_xO_4$, *Mater. Chem. Phys.*, *123*, 434–438.

Vidic, N. J., J. D. TenPas, K. L. Verosub, and M. J. Singer (2000), Separation of pedogenic and lithogenic components of magnetic susceptibility in the Chinese loess/palaeosol sequence as determined by the CBD procedure and a mixing analysis, *Geophys. J. Int.*, *142*, 551–562.

Wolska, E. (1981), The structure of hydrohematite, *Z. Kristallogr.*, *154*, 69–76.

Yang, T., J. Chen, H. Wang, and H. Jin (2012), Rock magnetic properties of fault rocks from the rupture of the 2008 Wenchuan earthquake, China and their implications: Preliminary results from the Zhaojiagou outcrop, Beichuan County (Sichuan), *Tectonophysics*, *530*, 331–341.

Yang, T., M. J. Dekkers, and B. Zhang (2016), Seismic heating signatures in the Japan Trench subduction plate-boundary fault zone: Evidence from a preliminary rock magnetic ‘geothermometer’, *Geophys. J. Int.*, *205*, 332–344.

Yu, Y., A. Mendoza-Garcia, B. Ning, and S. Sun (2013), Cobalt-substituted magnetite nanoparticles and their assembly into ferrimagnetic nanoparticle arrays, *Adv. Mater.*, *25*, 3090–3094.

Zélis, P. M., G. Pasquevich, S. Stewart, M. F. van Raap, J. Aphesteguy, I. Bruvera, C. Laborde, B. Pianciola, S. Jacobo, and F. Sánchez (2013), Structural and magnetic study of zinc-doped magnetite nanoparticles and ferrofluids for hyperthermia applications, *J. Phys. D*, *46*, 125006.

Zhang, C., G. A. Paterson, and Q. Liu (2012), A new mechanism for the magnetic enhancement of hematite during heating: The role of clay minerals, *Stud. Geophys. Geod.*, *56*, 1–16.

Zhao, X., D. Heslop, and A. P. Roberts (2015), A protocol for variable-resolution first-order reversal curve measurements, *Geochem. Geophys. Geosyst.*, *16*, 1–14, doi:10.1002/2014GC005680.

Zhou, L., F. Oldfield, A. Wintle, S. Robinson, and J. Wang (1990), Partly pedogenic origin of magnetic variations in Chinese loess, *Nature*, *346*, 737–739.

Zhou, W., R. Van der Voo, and D. R. Peacor (1997), Single-domain and superparamagnetic titanomagnetite with variable Ti content in young ocean-floor basalts: No evidence for rapid alteration, *Earth Planet. Sci. Lett.*, *150*, 353–362.